Journal of Physics D:
Applied Physics

PURPOSE-LED PUBLISHING™

PAPER • **OPEN ACCESS**

The harmonic residual index: a spectral purity metric for magnetic hyperthermia RF generators

To cite this article: Serhat Ilgaz Yöner *et al* 2026 *J. Phys. D: Appl. Phys.* **59** 355403

View the article online for updates and enhancements.

You may also like

- A multifrequency eletromagnetic applicator with an integrated AC magnetometer for magnetic hyperthermia experiments
E Garaio, J M Collantes, F Plazaola et al.
- Uncertainties in the estimation of specific absorption rate during radiofrequency alternating magnetic field induced non-adiabatic heating of ferrofluids
B B Lahiri, Surojit Ranoo and John Philip
- Experimental validation of hyperthermia SAR treatment planning using MR B_{1+} imaging
Cornelis A T Van den Berg, Lambertus W Bartels, Astrid A C De Leeuw et al.

This content was downloaded from IP address 193.140.199.113 on 07/11/2026 at 21:07

Journal of Physics D: Applied Physics

Check for updates

OPEN ACCESS

RECEIVED
26 March 2026

REVISED
11 August 2026

ACCEPTED FOR PUBLICATION
24 August 2026

PUBLISHED
3 September 2026

Original content from this work may be used under the terms of the Creative Commons Attribution 4.0 licence.

Any further distribution of this work must maintain attribution to the author(s) and the title of the work, journal citation and DOI.

PAPER

The harmonic residual index: a spectral purity metric for magnetic hyperthermia RF generators

Serhat Ilgaz Yöner[1,2,3,*], **Alpay Özcan**[3,4,5] and **Oğuz Akın**[6]

[1] Institute of Biomedical Engineering, Boğaziçi University, İstanbul 34342, Türkiye
[2] Department of Biomedical Equipment Technology, Vocational School, Acıbadem Mehmet Ali Aydınlar University, İstanbul 34752, Türkiye
[3] Electrical and Electronics Engineering Department, Boğaziçi University, İstanbul 34342, Türkiye
[4] Magnetic Medical Devices Laboratory, Boğaziçi University, İstanbul 34342, Türkiye
[5] Systems Science and Mathematics Laboratory, Boğaziçi University, İstanbul 34342, Türkiye
[6] Department of Radiology, Memorial Sloan Kettering Cancer Center, New York, NY, United States of America
[*] Author to whom any correspondence should be addressed.

E-mail: serhat.yoner@acibadem.edu.tr

Keywords: magnetic hyperthermia, electromagnetic safety, harmonic distortion, specific absorption rate, spectral purity, radiofrequency characterization

Supplementary material for this article is available online

Abstract

RF generators are core components of magnetic hyperthermia (MH) systems, yet output quality is rarely characterized beyond nominal frequency and amplitude. Harmonic distortion can introduce parasitic components that complicate reproducibility and accurate field characterization; MH-specific spectral quality indices remain limited. This study proposes two indices for RF generator output quality assessment in MH: the harmonic residual index (HRI) and a simulation-derived harmonic specific absorption rate (SAR) contribution index ($\bar{\Lambda}_{SAR}$). A sinusoidal RF generator (50–200 kHz, 115 W) was evaluated with three coil configurations at 10%–100% power. Spatial magnetic-field measurements were acquired using a passive search coil, and HRI was computed pointwise to generate harmonic distortion maps. THD was computed from the same spectra for benchmarking. Spatial mean HRI ($\overline{HRI}$) and THD ($\overline{THD}$) were modelled using weighted power-law fitting. Inductive heating experiments (120–166.5 mg ml^{-1} MNP) evaluated the reliability of experimental calorimetry, motivating a shift toward simulation-based dosimetry. Finite element method (FEM) simulations of a simplified neck model driven by measured harmonics estimated relative harmonic SAR contributions and $\bar{\Lambda}_{SAR}$. $\overline{HRI}$ ranged from 0.17 ± 0.04 to 16.41 ± 3.48 (RMSE = 0.301–1.523) and increased monotonically with power level across all coils, while THD showed smaller variations and less spatially structured behaviour. Experimental heating trials yielded marginal temperature elevations ($\leqslant$2.5 °C) with quantization errors, demonstrating that standard calorimetry is metrologically insufficient for SAR derivation at clinical field intensities. Conversely $\bar{\Lambda}_{SAR}$ ranged from 2.23E + 4 to 2.70E + 6, indicating low harmonic contributions relative to the fundamental under the tested conditions. HRI enables spatially resolved quantification of RF generator spectral impurities in MH systems and provides greater spatial sensitivity than THD under the tested conditions. Combined with FEM screening of harmonic SAR contributions, the framework supports reproducible, standardized characterization of RF generator output quality for MH instrumentation quality assurance.

Glossary

ABS	Acrylonitrile butadiene styrene
AC	Alternating current
AMF	Alternating magnetic field

© 2026 The Author(s). Published by IOP Publishing Ltd

BNC	Bayonet Neill–Concelman
CSL	Cervical skin layer
FEM	Finite element method
FFT	Fast Fourier transform
HRI	Harmonic residual index
HWRW	Helmholtz coil with round wire
ILP	Intrinsic loss parameter
MH	Magnetic hyperthermia
MNP	Magnetic nanoparticle
MRI	Magnetic resonance imaging
NMT	Neck muscle tissue
PID	Proportional–Integral–Derivative
RBM	Red bone marrow
RMS	Root mean square
RMSE	Root mean square error
SAR	Specific absorption rate
SNR	Signal-to-noise ratio
SPION	Superparamagnetic iron oxide nanoparticle
SWLW	Solenoid coil with Litz wire
SWRW	Solenoid coil with round wire
THD	Total harmonic distortion
VCB	Vertebral cortical bone

1. Introduction

MH is a localized cancer therapy that employs AMF in the 100–400 kHz range to heat magnetic nanoparticles (MNP), thereby delivering controlled thermal doses that selectively destroy tumour cells [1–3]. By restricting heating to MNP-loaded regions, MH enables precise thermal dosing in anatomically constrained regions, making it particularly promising for head and neck tumours, where surrounding critical structures limit conventional therapies [4, 5]. Preclinical and early clinical studies have demonstrated effective intratumoral heating, reinforcing its potential as a safe targeted therapeutic modality [6, 7].

The performance of MH critically depends on the characteristics of the RF generators that drive the RF coils producing the AMFs. RF generator design, including impedance-matching with the RF coil, output stability, and spectral purity directly affects the efficiency of MNP heating and the spatial precision of thermal delivery [8–10]. Imprecise or unstable output can degrade spectral purity, diverting energy from the fundamental frequency into harmonic components that do not contribute to therapeutic MNP heating, reducing the overall efficiency of energy delivery [11, 12].

However, beyond general stability, the spectral composition of the waveform plays a decisive role in the balance between therapeutic heating and parasitic energy losses [13]. Harmonic content represents a non-therapeutic drain on the generator's energy budget; because eddy-current losses scale approximately with the square of frequency (f^2) [14, 15], higher-order harmonics dissipate energy disproportionately relative to their amplitude, coupling primarily into eddy-current losses within the generator, coil, and surrounding conductive hardware rather than into the therapeutic MNP heating pathway [16–18]. In systems with high harmonic distortion, the RF generator must be driven to higher total power levels to achieve a target MNP temperature, degrading the therapeutic efficiency, defined as the ratio of MNP heating to total eddy-induced power. By minimizing this non-therapeutic energy loss, spectral control may help improve the overall efficiency and predictability of the delivered dose. This system-level parasitic dissipation occurring in the coil windings, matching network, and surrounding conductive structures, is distinct from, and generally much larger than, the fraction of harmonic energy that couples specifically into patient-adjacent tissue.

Moreover, as MH transitions toward clinical application, the need for standardized performance metrics is becoming increasingly important [19, 20]. Biomedical standards for high-frequency medical

devices, such as MRI systems [21] and electrosurgical units [22], emphasize the exhaustive characterization of electromagnetic outputs to ensure patient and operator safety [23], particularly regarding unintentional field exposure [24–26]. While MH currently lacks an equivalent framework, the development of standardized spectral purity metrics represents a pathway toward addressing current dosimetric uncertainties. Quantifying the spectral purity of the RF generator provides a useful framework for standardized characterization of MH hardware, supporting reproducibility and providing a foundation for future dosimetric and regulatory frameworks as the field matures [20].

Although the role of RF generator output quality is under-explored, there are a few relevant but distinct lines of work. First, Zeinoun *et al* demonstrated that non-sinusoidal waveforms, specifically trapezoidal and almost-square shapes, can significantly improve MNP heating efficiency compared to classical sinusoidal excitation [27]. Second, Barrera *et al* showed that a tuneable trapezoidal waveform can fine-tune the temperature profile in MH, by adjusting a taper parameter of the waveform, thereby improving thermal control and initial transients [28]. Third, Sharma *et al* developed a PID-controlled MH system with real-time temperature feedback, driving an RF coil at 160 kHz and validating the approach *in vivo* with continuous temperature monitoring and regulation [29]. However, none of these studies systematically characterize or standardize the RF generator output signal quality (i.e. spectral purity, harmonic distortion, field stability) independent of RF coil or MNP parameters. Waveform-optimization and control systems focus on improving heating or regulating temperature, but do not provide a framework for quantifying RF generator performance. Our work addresses this gap by introducing rigorous metrics and measurement procedures for assessing RF generator signal quality to optimize both heating efficiency and reproducibility.

The development of such a framework is particularly critical as MH systems often operate at relatively low magnetic field intensities (5–10 kA m^{-1}) for avoiding side effects [30]. These levels result in slow heating patterns that are highly susceptible to thermal noise and environmental heat flux [31]. In this regime, slow heating patterns and resolution limits of fibre-optics based experimental calorimetry [32] can render SAR calculations unreliable, as subtle dosimetric shifts from both fundamental and harmonic components are often masked by the system's thermal dynamics. This 'thermal blindness' necessitates a shift toward high-fidelity computational modelling, guided by a rigorous spectral metric, to accurately resolve the spatial redistribution of induced fields.

In this study, we propose a reproducible framework for evaluating and optimizing RF generator output quality in MH systems by quantifying spectral purity, harmonic content, and spatial field stability, while benchmarking the proposed metric against the established total harmonic distortion (THD), to improve heating efficiency and reproducibility.

2. Methods

The methodological workflow consisted of five main stages: RF generator design, impedance-matching board development, magnetic field measurements, formulation of the HRI, and FEM simulations for tissue SAR estimation. The RF coils; SWRW, SWLW, and HWRW used for generating MH magnetic fields, as well as the passive search coil and spatial positioning grid used for magnetic field measurements, were developed during the author's doctoral studies [33]. The three RF coil geometries were selected as representative configurations to span different field distribution and coupling regimes commonly encountered in MH systems [34, 35]. Additional data were provided in the supplementary materials.

2.1. Radiofrequency generator

A low-frequency RF generator capable of delivering stable AMF signals within the 50–200 kHz range and up to 115 W was designed to drive the RF coils (figures 1, S1–S2). The system was powered by two identical switched-mode power supplies (SMPS, UHP-750-48, Mean Well, New Taipei City, Taiwan), each rated at 750 W and 24 V, providing symmetrical ±24 V to the oscillator and amplifier stages.

A Wien–Bridge oscillator topology was selected for generating low-distortion sinusoidal signals [36]. Instead of two separate resistors, a stereo potentiometer was used in the feedback network, providing symmetric control over the oscillation frequency. The oscillator stage was cascaded with a Class AB amplifier to achieve high output power.

A secondary OPA541AP served as a buffer between the oscillator and amplifier stages, converting the high-impedance, low-current signal into a low-impedance, high-current drive [37]. A voltage divider, consisting of a potentiometer and a fixed resistor was implemented between the oscillator output and buffer input to provide adjustable amplitude control within the 0–24 V range. Direct current (DC)-blocking capacitors were placed at the interface to prevent bias coupling and offset propagation [38].

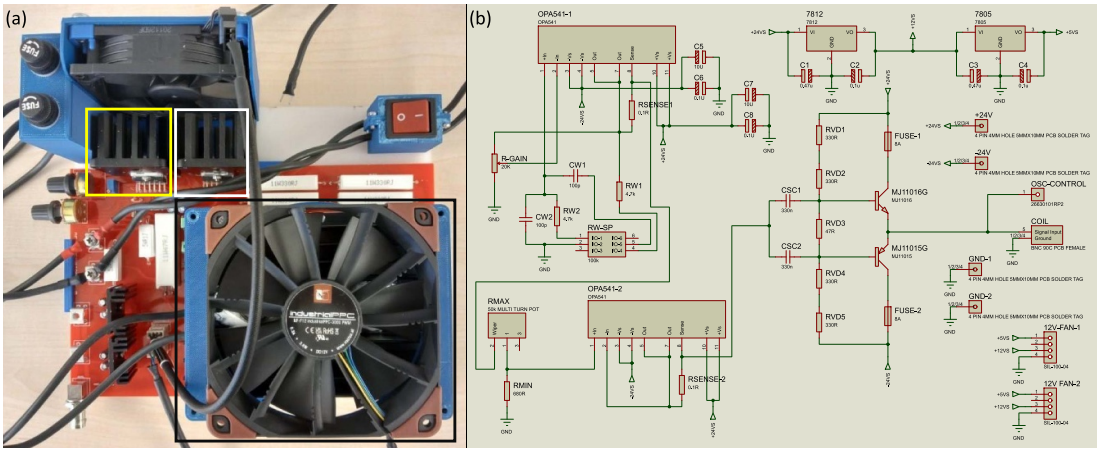

Figure 1. (a) Top view of the designed RF generator. The yellow rectangle indicates the oscillator stage centred around a OPA541AP power OP-AMP with its dedicated heat sink, and the white rectangle highlights the pre-amplification stage OPA541AP OP-AMP with its dedicated heat sink, both sharing a medium sized cooling fan. The black rectangle identifies the final power amplification stage, comprising a high-current Darlington transistor pair; these components, along with their primary heat sinks, are situated beneath the large sized cooling fan to ensure stable thermal operation during continuous 150 kHz induction. (b) schematic drawing of the whole RF generator circuit.

In the Class AB amplifier, the positive and negative half-cycles of the sinusoidal waveform were amplified using MJ11016G and MJ11015G Darlington transistors (On Semiconductor, Phoenix, AZ, USA) respectively, selected for their high-power and high-gain characteristics. 11 W sandstone power resistors were employed for DC biasing of the transistors to maintain thermal stability and improve amplifier efficiency, and 8 A ceramic fuses were placed in series with the collector supply connections of the transistors to provide circuit protection.

The printed circuit board was designed using the EAGLE (Autodesk, San Francisco, CA, USA) environment in compliance with IPC-2221 standards [33]. Thermal management was implemented using aluminium heat sinks (680–125 220 and 413 K models, Wakefield-Vette, Nashua, NH, USA) and active cooling fans (NF-A9 PWM Chromax and NF-F12 Industrial PPC, Noctua, Vienna, Austria). Silicone-based thermal paste with metal oxide filler (DLG, İstanbul, Türkiye) ensured minimal thermal resistance between components and heat sinks. A rocker switch was integrated for rapid on/off state control, and custom parts were designed and 3D-printed from high-temperature ABS to mount the cooling fans, the rocker switch and serve as enclosure for the ceramic fuses, improving mechanical stability and operator safety.

2.2. Impedance-matching board

The impedance-matching between the RF generator and the three RF coils (figure 2, tables S1–S2) was implemented at 150 kHz via a custom-designed board consisting three distinct, switchable, high-pass L-networks [39], mounted on a single board. A three-way slider switch enabled seamless selection of the appropriate L-network to match the unique load impedance (table S3).

All connections utilized standard 50 Ω BNC connectors and RG-213 coaxial cable to maintain optimal signal shielding and transmission line integrity. However, to maximize current delivery into the RF coils and ensure maximum power transfer, the impedance-matching networks were designed based on the RF generator's low, measured internal output impedance rather than the nominal 50 Ω characteristic impedance [40].

2.3. Magnetic field measurements

Magnetic field measurements relied on Faraday's Law of Induction [41], a passive search coil was used to track the time-varying magnetic fields. The electromagnetically induced voltages on the passive search coil were measured using DS1102E model oscilloscope (Rigol, Beijing, China). Absolute calibration of the passive search coil is not required because the measurement chain acts as an intrinsically self-compensating system, where the $1/f$ reduction in harmonic current within the inductive load is balanced by the f -proportional voltage induction of the passive search coil, ensuring that measured spectral ratios directly reflect the generator's output quality. Also, harmonic analysis was restricted to frequency components well below the self-resonant frequency of the passive search coil and within the acquisition bandwidth of the oscilloscope. Multiple passive search coils were tested; the final passive search coil was an

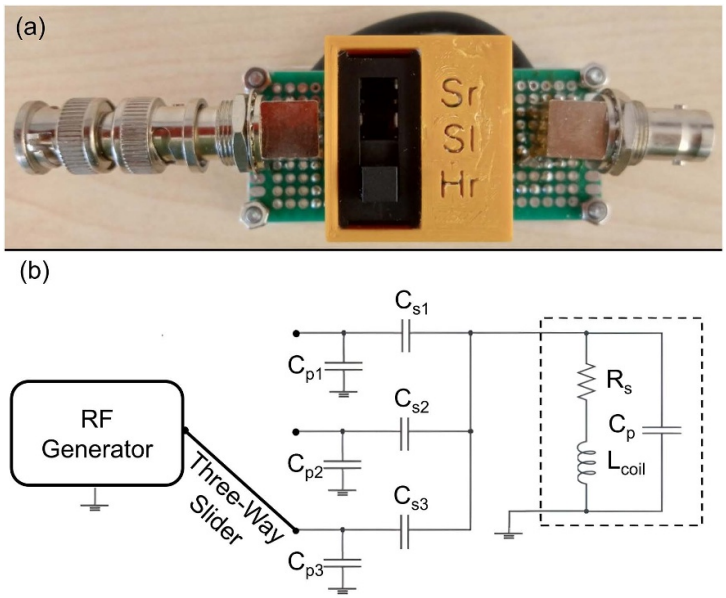

Figure 2. (a) Top-view photograph of the fabricated impedance-matching board, with the three-way slider set to the HWRW configuration. (b) Schematic drawing of the L-network impedance-matching circuit, connected to the RF generator via the three-way slider and connected to the RLC equivalent RF coil load. The series–parallel capacitor pairs C_{s1}–C_{p1}, C_{s2}–C_{p2}, and C_{s3}–C_{p3} corresponding to the impedance-matching lines for SWRW, SWLW, and HWRW, respectively.

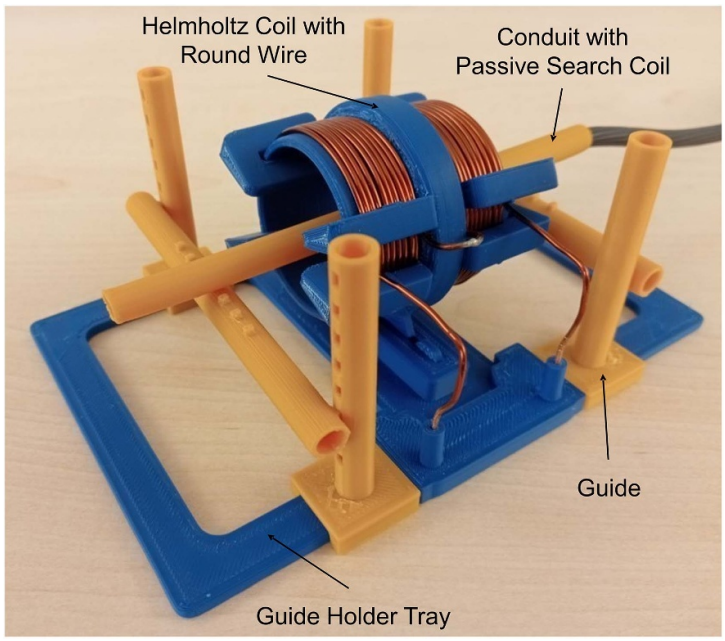

Figure 3. In-house designed and 3D printed ABS guide frame; conduit with passive search coil, guide and guide holder tray with Helmholtz coil with round wire.

in-house fabricated, single-turn passive search coil with a 6 mm diameter (figure S3). The design and selection criteria for the passive search coil were optimized to be the minimal diameter while satisfying mean SNR greater than 10. This SNR $>$ 10 criterion was defined as the mean SNR computed across all five power levels: 100%, 75%, 50%, 25%, and 10% of the HWRW (table S4). This combination of criteria was chosen as the optimal compromise between achieving enhanced spatial resolution and maintaining adequate measurement fidelity. For holding the passive search coils and wiring in place, conduit structures were designed and 3D printed from ABS.

To ensure consistent and repeatable spatial positioning of the passive search coil, an in-house designed guide frame was fabricated via 3D printing from ABS. This guide frame served to fixate and displace the passive search coil inside the three RF coils under test (figure 3). The guide frame provides

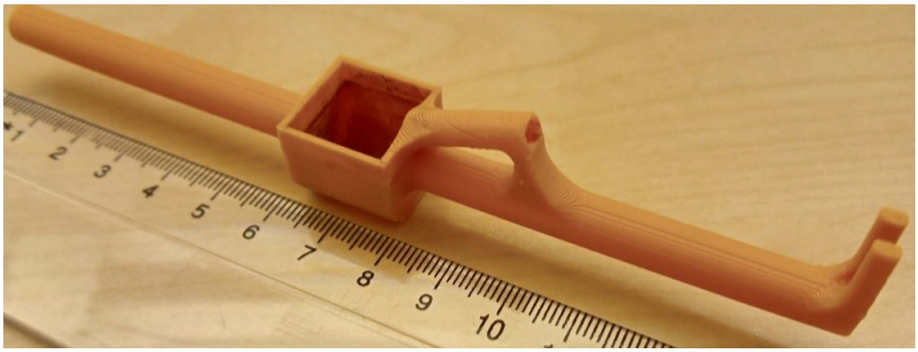

Figure 4. In-house designed and 3D printed ABS cup designed to contain MNPs during MH measurements.

precise displacement capability in each direction with 6 mm steps. Measurements were conducted across a total of 63 spatial positions for each RF coil. This grid comprised 21 transversal and 3 axial positions, all separated by 6 mm steps. The entire measurement campaign was repeated at five power levels previously defined in the study protocol, corresponding to 6.5 A RMS current for SWRW and SWLW, 4.5 A RMS current for HWRW at 100% power level at 150 kHz. The system noise was measured from the centre of each RF coil while the RF generator output signal was set to zero ($I_{\mathrm{Coil}} = 0$).

2.4. Inductive heating measurements

To evaluate the inductive heating performance, SPION samples were prepared at a stock concentration of 166.5 mg ml^{-1}. The nanoparticles consist of 13 nm diameter iron oxide cores stabilized with a β-cyclodextrin coating and dispersed in distilled water (Electrical conductivity = 1.2 μS cm^{-1}). Morphological characterization via scanning transmission electron microscopy (ESEM, Quattro S, Thermo Fisher Scientific, USA) confirmed an average core diameter of 13 nm, while dynamic light scattering (Zetasizer Nano S90, Malvern Panalytical, UK) indicated an average hydrodynamic diameter of 52 nm. For concentration-dependent analysis, a subset of the samples was diluted with distilled water to 120 mg ml^{-1}.

Experimental calorimetry was conducted using a custom-engineered 4.096 ml ABS cubic holder (figure 4), featuring integrated guide frames for precise fibre-optic probe alignment within the RF coils. Thermal dynamics were tracked using a high-field-compatible GaAs fibre-optic temperature sensor (TS2, Weidmann-Optocon, Germany) paired with a FOTEMP OEM signal conditioner and FOTEMP Assistant 2 software. Data acquisition was performed at a sampling period of 250 ms, with subsequent post-processing executed in MATLAB (v24.2, MathWorks Inc., Portola Valley, CA, USA). To evaluate the thermal dynamics of the system, 2 ml MNP samples were positioned at the geometric centre of the RF coil, representing the theoretical region of maximum field uniformity. Measurements were conducted across both concentration levels (120 and 166.5 mg ml^{-1}) to observe the heating response under the 150 kHz fundamental frequency at 100% generator power level. Each trial was recorded for 40 min to capture the complete thermal response and verify temperature stabilization. Preliminary observations showed that heating approached a plateau after approximately 30–35 min; therefore, an additional 5–10 min was included to confirm steady-state behaviour. To ensure reproducible initial conditions, all experiments commenced at an ambient temperature of 22 °C (±0.1 °C), with mandatory cooling intervals between trials to allow the RF coil to return to thermal equilibrium. Baseline control experiments were performed using the same cubic holder filled with distilled water to isolate non-specific heating effects from the fundamental and harmonic field components. This protocol was specifically designed to evaluate the SNR limitations of experimental calorimetry at 150 kHz, providing a baseline to demonstrate the unreliability of SAR computations derived from low-intensity inductive heating in the presence of environmental heat flux.

To quantify these limitations, the background environmental contribution to the total observed temperature rise, *BC*, was defined for each coil and MNP concentration as:

$$BC = \frac{|\Delta T_{\mathrm{Control}}|}{|\Delta T_{\mathrm{MNP}}|} \times 100 \tag{1}$$

where in, $\Delta T_{\mathrm{Control}}$ is the temperature change of the distilled water control over the measurement window, and ΔT_{MNP} is the total temperature change of the corresponding MNP suspension over the same

window. The effective temporal resolution of the calorimetric measurement was characterized via the number of resolvable discrete temperature increments, N_{Steps}, defined as:

$$N_{\text{Steps}} = \left|\text{unique}\left(\text{round}\left(\frac{T(t)}{\delta T}\right)\right)\right| - 1 \tag{2}$$

where in, $T(t)$ is the recorded temperature trace, δT is the sensor resolution (0.1 °C), and unique$(\cdot)$ denotes the count of distinct quantized levels observed over the measurement window. The corresponding mean step interval, τ_{Steps}, was calculated as:

$$\tau_{\text{Steps}} = \frac{t_{\text{Window}}}{N_{\text{Steps}}}. \tag{3}$$

As a standard benchmark, SAR was additionally estimated using the initial-slope method commonly applied in MH calorimetry [31]:

$$\text{SAR} = c_p \frac{m_{\text{Sample}}}{m_{\text{Fe}}}\left(\frac{\mathrm{d}T}{\mathrm{d}t}\right)_{t\to 0} \tag{4}$$

where in, c_p is the specific heat capacity of the sample (approximated as that of water, 4186 J $(\text{kg}\cdot\text{K})^{-1}$, valid for dilute suspensions), m_{Sample} and m_{Fe} are the total sample mass and magnetic (iron oxide) mass, respectively, and $(\mathrm{d}T/\mathrm{d}t)_{t\to 0}$ is the initial heating slope, estimated via linear regression over the first 90 s of each trial to minimize confounding from environmental heat exchange, consistent with standard practice for reducing the influence of convective and conductive losses at longer timescales [31]. The mass ratio was calculated from the nominal MNP (iron oxide) mass concentration (120 or 166.5 mg ml^{-1}), assuming a sample density of $\approx$1 g ml^{-1} consistent with the dilute aqueous suspensions used (13 nm core diameter, 52 nm hydrodynamic diameter, β-cyclodextrin coating).

2.5. HRI

HRI index was proposed to quantify and comparatively analyse the spectral purity of the AC generated by the RF generator, relying on the three RF coil AMFs. This index provides a single-value measure of signal quality by factoring in both the distortion arising from the RF generator's non-linearities and the constant system-level noise. All recorded time-domain magnetic field measurements were transferred directly from the oscilloscope memory to the analysis computer and subsequently imported into MATLAB for an initial FFT analysis to retrieve amplitudes of fundamental and harmonic frequencies.

The HRI is governed by two primary variables and formula is as follows:

$$\text{HRI}(r) = \frac{S(r)}{N_T(r)} \tag{5}$$

where in, r is one of 63 spatial measurement coordinates, $S(r)$ and $N_T(r)$ are the spatially dependent signal power quantity and total noise power quantity variables, respectively. $S(r)$ is defined as:

$$S(r) = \left(|V_{1,\text{RMS}}(r)|\right)^2 \tag{6}$$

and is calculated over spatially dependent RMS voltage, $V_{1,\text{RMS}}(r)$ of the fundamental frequency 150 kHz. While $N_T(r)$ is defined as:

$$N_T(r) = N_H(r) + N_S. \tag{7}$$

Where in, $N_H(r)$ and N_S are spatially dependent harmonic noise power quantity and the constant system noise power quantity variables, respectively. $N_H(r)$ is formulated as:

$$N_H(r) = \sum_{i=3,5,\ldots}^{\max} \left(|V_{i,\text{RMS}}(r)| \times i\right)^2 \tag{8}$$

which is based on the spatially dependent RMS voltages, $V_{i,\text{RMS}}(r)$ of the odd-harmonics ($i = 3,5,\ldots$). Absolute of each harmonic signal is weighted by the integer harmonic order (i) through multiplication. The odd-harmonics ($i = 3,5,\ldots$) based formula specifically targets the asymmetrical distortion characteristic of the Class AB push–pull amplifier architecture [42], and weighting each harmonic signal by its integer harmonic order (i) is done for penalizing higher frequencies more severely due to their potential for increased parasitic effects and greater coupling with biological tissues [43]. Even-order harmonics

were fully measured in the spectral data but are not included in the HRI formulation, as the metric is specifically defined to capture the dominant asymmetrical distortion component of the Class AB amplifier output. Finally, system noise measurements conducted under the condition $I_{\text{Coil}} = 0$ were used for calculating:

$$N_S = (|\sigma_{\text{noise}}|)^2 \tag{9}$$

where in, σ_{noise} is the system noise in the form of standard deviation due to statistical nature of the quiescent system noise [44]. At each of the previously defined power levels, for each RF coil, spatially mean HRI is calculated as follows:

$$\overline{\text{HRI}} = \frac{1}{63}\sum_{r=1}^{63}\text{HRI}(r) \tag{10}$$

where in, the limits of the summation are bounded by total number of spatial measurement positions. $\overline{\text{HRI}}$ is selected as the primary index for the subsequent inter-coil and inter-power level comparative analysis. Relationship between $\overline{\text{HRI}}$ and previously defined power levels were modelled for each RF coil. A mix of statistical and machine learning-based algorithms: power-law (log-linearized with smearing factor correction), third-order polynomial, ridge regression (L_2 penalized the model with $\lambda = 1$), and smoothing spline were tested in MATLAB, with predictive performance assessed via 5-fold cross-validation (CV). Model selection was based on minimizing the RMSE, calculated as the mean of the 5-fold CV scores. For visual analysis of HRI and $\overline{\text{HRI}}$, 3D slice maps and 2D plots were generated in MATLAB, respectively.

To benchmark the proposed HRI against a conventional spectral distortion metric, THD was also computed. THD is a commonly used spectral purity measure defined as the ratio of the RMS sum of harmonic components to the RMS amplitude of the fundamental component. In this study, THD was calculated from the same FFT-derived harmonic amplitudes used in HRI, according to:

$$\text{THD}(r) = \frac{\sqrt{\sum_{k=2}^{\max} V_{k,\text{rms}}^2(r)}}{V_{1,\text{rms}}(r)} \tag{11}$$

where V_1 denotes the RMS amplitude of the fundamental frequency component and V_k denotes the RMS amplitude of the kth harmonic component. Since both HRI and THD were computed pointwise across the spatial measurement grid, the spatially mean THD ($\overline{\text{THD}}$) was also calculated for each RF coil and power level to enable direct comparison with HRI:

$$\overline{\text{THD}} = \frac{1}{63}\sum_{r=1}^{63}\text{THD}(r). \tag{12}$$

Mean and standard deviation values of the HRI and THD indices were reported to represent spatial variability of the derived spectral metrics obtained from deterministic sampling across 63 discrete spatial positions for each configuration. These statistical descriptors therefore reflect spatial distribution of the computed indices within each RF coil system rather than repeated measurements of independent experimental realizations. Consequently, the dataset does not satisfy the assumptions of independent and identically distributed samples required for classical inferential statistical tests such as ANOVA. Comparisons across coil types and power levels were therefore based on descriptive spatial trends and regression analysis of power-dependent aggregated indices.

2.6. SAR simulations

FEM based COMSOL Multiphysics (v.5.5, COMSOL AB, Stockholm, Sweden) simulations exposed a human neck model to the same experimentally measured fundamental and harmonic frequencies to compute SAR for each tissue. Simulation was chosen over experimental thermometry to provide a stable, non-invasive environment for energy absorption mapping. This approach isolates SAR as a pure metrological variable, independent of confounding ambient thermodynamic factors such as ambient convection and heat diffusion [45]. All simulations were conducted at 2D-axisymmetric space due to RF coils' inherent axisymmetric geometry for computational efficiency and accuracy [46].

The three RF coils were constructed within the FEM environment according to their actual physical dimensions (figure S2). Subsequently, a miniaturized cylindrical human neck model was added to the domain, centred at the inner coil gap. This model comprised four distinct tissue layers with specified

thicknesses: red bone marrow (RBM: 8 mm), vertebral cortical bone (VCB: 2.25 mm), neck muscle tissue (NMT: 10 mm), and cervical skin layer (CSL: 2.5 mm). The simulation geometries were discretized using free triangular elements, with minimum and maximum element sizes of 0.02 and 10 mm, respectively. To better capture near-surface effects along the coil wires, a boundary layer mesh was applied to the wire edges, consisting of 12 layers with a stretching factor of 1.2. This meshing strategy ensured improved numerical accuracy and allowed the generation of high-resolution current density distributions throughout the coil geometry.

Electrical conductivity, relative permittivity and relative permeability material properties were assigned to each domain (table S5), values sourced from Total Materia Database [47]. Magnetic Fields module was used for electric field computations of each point in space, to this end, COMSOL Multiphysics relies on time-harmonic form of Faraday's law:

$$E = -\mathrm{j}\omega A \tag{13}$$

where in, j is the imaginary unit indicating a 90° phase shift between the magnetic and electric fields in the phasor form, ω is the angular frequency proportional to the oscillation rate of the magnetic field, and A is the magnetic vector potential. Then, inserting E to the formula:

$$Q_{\mathrm{rh}} = \frac{1}{2}\kappa|E|^2 \tag{14}$$

where in, κ is the electrical conductivity, program computes time-averaged volumetric electric loss density (Q_{rh}). Finally, spatially mean SAR for each tissue domain is computed:

$$\overline{\mathrm{SAR}} = \frac{1}{V}\int_V \left(\frac{Q_{\mathrm{rh}}}{\rho}\right)\mathrm{d}V, \tag{15}$$

where in, ρ is the tissue density, V is tissue domain volume, and dV is the infinitesimal volume element used in the integration.

Coil domain boundary condition was assigned to the constructed RF coils, with conductor model and coil excitation properties set to 'single conductor' and 'current,' respectively. Previously defined 6.5 A RMS for SWRW and SWLW, 4.5 A RMS for HWRW were applied as fundamental frequency (150 kHz) current inputs at 100% power level, and a Frequency Domain study was employed, yielding $\overline{\mathrm{SAR}}$ originating from the fundamental frequency $\overline{\mathrm{SAR}}_1$. Then, each experimental $V_{i,\mathrm{RMS}}$ value, corresponding to spatial centre of the RF coil was converted to harmonic current amplitudes $I_{i,\mathrm{RMS}}$ by dividing by the RF coil impedances (table S1). All and harmonic frequencies f_i were imported into COMSOL Multiphysics as an interpolation table, and a combined Frequency Domain and Parametric Sweep study was conducted to automate the electric field computation for all $I_{i,\mathrm{RMS}}$ and f_i inputs. As the post processing, $\overline{\mathrm{SAR}}$ originating from all f_i ($\overline{\mathrm{SAR}}_i$) for each tissue domain were superimposed for computing total $\overline{\mathrm{SAR}}$ originating from all odd-harmonic signals:

$$\overline{\mathrm{SAR}}_H = \sum_{i=3,5,\ldots}^{\max} \overline{\mathrm{SAR}}_i \tag{16}$$

and SAR Quality Index across $\overline{\mathrm{SAR}}$ was defined as:

$$\bar{\Lambda}_{\mathrm{SAR}} = \frac{\overline{\mathrm{SAR}}_1}{\overline{\mathrm{SAR}}_H}. \tag{17}$$

Simulations were repeated for previously defined power levels. For visual analysis of $\overline{\mathrm{SAR}}_1$ and $\bar{\Lambda}_H$, grouped bar charts were generated.

3. Results

At the 100% power level, HRI (higher values indicate better spectral purity) ranged from 2.593 to 14.838, 3.631 to 9.931, and 10.781to 25.288 for the SWRW, SWLW, and HWRW, respectively (figure 5(a,c,e)). Measurement uncertainty is primarily governed by oscilloscope vertical accuracy (±3% of reading), while timebase uncertainty (±50 ppm) has a negligible effect on harmonic frequency placement and ratio-based metrics. FFT, HRI, and THD were computed offline from identical digitized waveforms, so spectral processing introduces no additional stochastic uncertainty, and FFT resolution is fixed

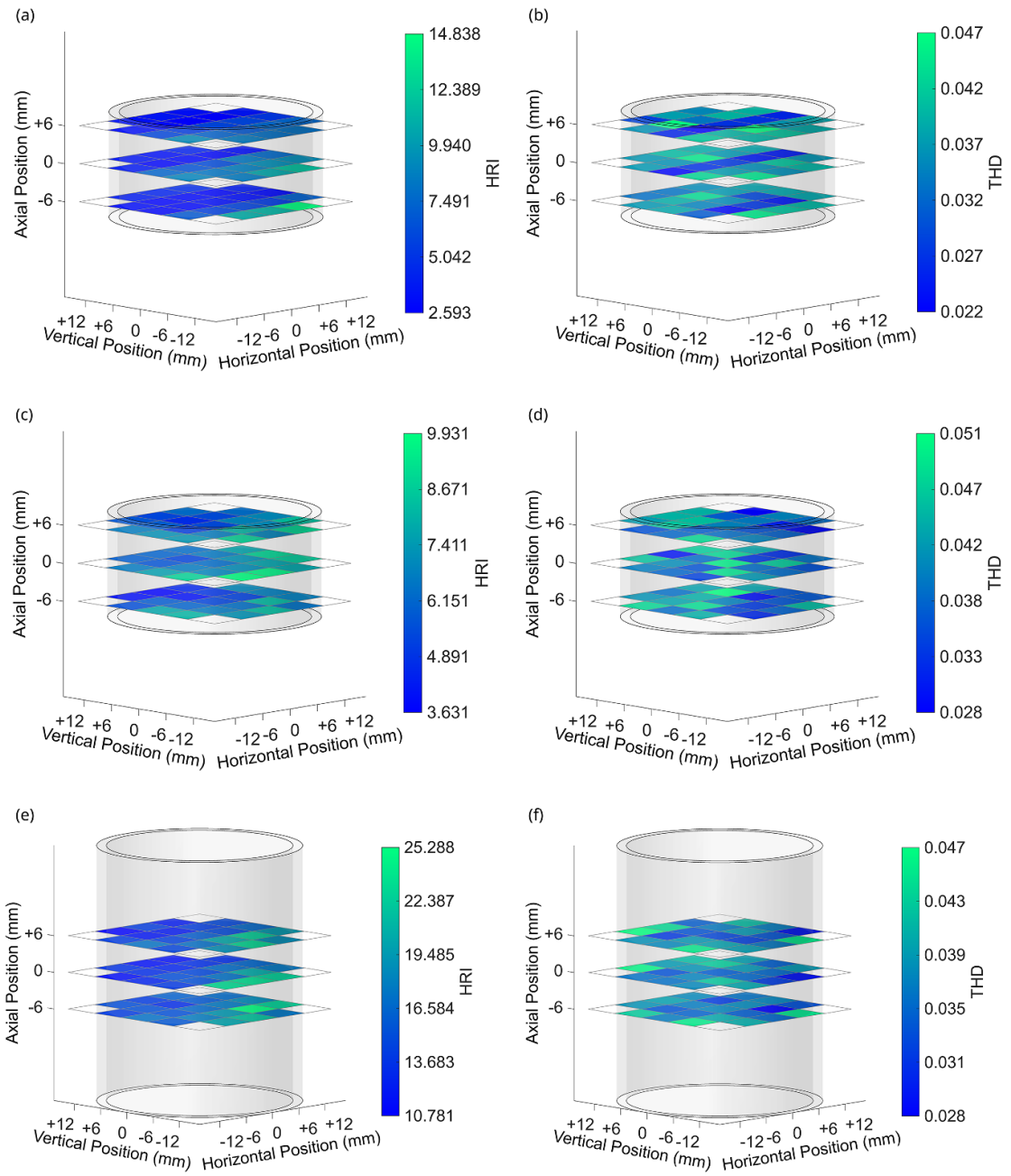

Figure 5. 3D slice maps of HRI for (a) SWRW, (c) SWLW, and (e) HWRW, and of THD for (b) SWRW, (d) SWLW, and (f) HWRW at 100% power level.

by $\Delta f = f\,\mathrm{s\ N^{-1}}$. Spatial mapping is constrained by a mechanical 3D guide system with 6 mm resolution in x, y, and z directions, defining the discretization limit of the measurements. Each acquisition corresponds to a steady-state 150 kHz excitation spanning multiple cycles, ensuring temporal stationarity and minimizing cycle-to-cycle variability. Overall, these uncertainties are small compared to the observed spatial and power-dependent variations in HRI and THD. Across all three coil geometries, HRI increased consistently from +12 to −12 mm along the vertical axis. In contrast, at the 100% power level, THD (lower values indicate better spectral purity) ranged from 0.022 to 0.047, 0.028 to 0.051, and 0.028 to 0.047 for the SWRW, SWLW, and HWRW, respectively (figure 5(b,d,f)), and exhibited a more spatially irregular distribution. HRI and THD maps for all power levels are provided in Figures S4–S6, and Figures S7–S9, respectively.

$\overline{\mathrm{HRI}}$ (Higher values indicate better spectral purity) increased at higher power level for all three RF coils, while the associated standard deviation also increased (table 1 and figure 6(a, c, e)). In contrast,

Table 1. $\overline{\text{HRI}}$ and $\overline{\text{THD}}$ data for three RF coils at all power levels.

Metric	Coil type	Power levels (%)				
		100	75	50	25	10
$\overline{\text{HRI}}$	SWRW	5.793 ± 2.836	3.476 ± 0.892	2.251 ± 0.695	1.186 ± 0.369	0.220 ± 0.083
	SWLW	6.699 ± 1.374	2.870 ± 0.720	2.206 ± 0.297	1.006 ± 0.268	0.172 ± 0.043
	HWRW	16.413 ± 3.480	7.779 ± 2.942	5.453 ± 1.388	1.204 ± 0.291	0.482 ± 0.132
$\overline{\text{THD}}$	SWRW	0.035 ± 0.006	0.043 ± 0.003	0.054 ± 0.003	0.065 ± 0.006	0.080 ± 0.020
	SWLW	0.040 ± 0.005	0.052 ± 0.005	0.049 ± 0.006	0.058 ± 0.007	0.087 ± 0.018
	HWRW	0.038 ± 0.004	0.043 ± 0.008	0.041 ± 0.005	0.035 ± 0.006	0.050 ± 0.010

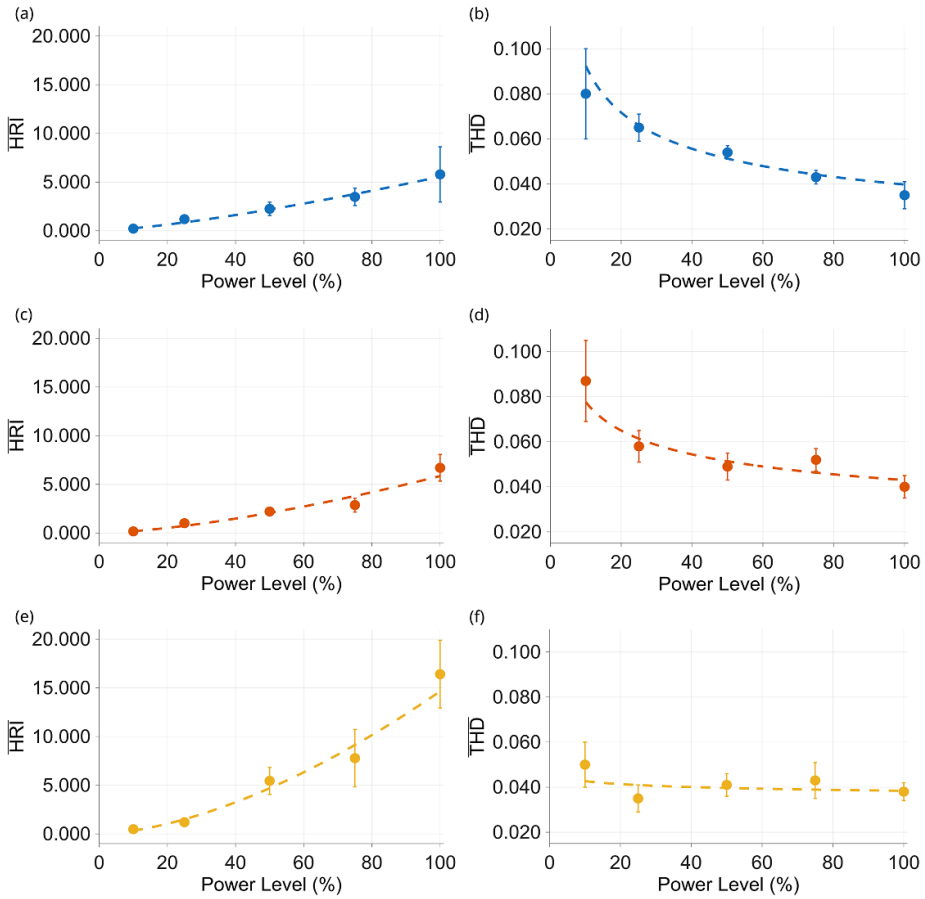

Figure 6. 2D Data and model predictions of $\overline{\text{HRI}}$ as a function of RF generator power level for (a) SWRW, (c) SWLW, and (e) HWRW. Corresponding results are shown for (b) SWRW, (d) SWLW, and (f) HWRW.

$\overline{\text{THD}}$ (lower values indicate better spectral purity) decreased with increasing power level for all three RF coils, while its standard deviation varied non-monotonically (table 1 and figure 6(b, d, f)). The power–law model, expressed as (y stands for $\overline{\text{HRI}}$ or $\overline{\text{THD}}$, while x stands for % power levels) was selected for predicting $\overline{\text{HRI}}$ and $\overline{\text{THD}}$ (figure 6) due to its low error rate without overfitting (table 2) and its ability to capture consistent monotonic scaling behaviour across power levels. The fitted $\overline{\text{HRI}}$ coefficients were $a = 0.013$, $b = 1.321$ for SWRW; $a = 0.007$, $b = 1.448$ for SWLW; and $a = 0.010$, $b = 1.571$ for HWRW. The fitted $\overline{\text{THD}}$ coefficients were $a = 0.215$, $b = -0.366$ for SWRW; $a = 0.140$, $b = -0.256$ for SWLW; and $a = 0.047$, for HWRW.

For the inductive heating measurements, 40 min thermal profiles for the control and MNP suspensions are shown in figures 7(a)–(c), evaluated to assess the metrological reliability of experimental calorimetry at clinical field intensities rather than to derive clinically representative SAR values. For the distilled water control (figure 7(a)), all RF coils maintained high stability between 21.9 °C and 22.0 °C, with fluctuations corresponding to the 0.1 °C fibre-optic temperature measurement system resolution. For the 120 mg ml^{-1} concentration (figure 7(b)), temperature elevations were recorded for the SWRW, SWLW, and HWRW coils as rising from 22.1 °C to 23.9 °C (1.8 °C rise), 22.1 °C to 23.5 °C

Table 2. Mean RMSE values for algorithms used for modelling power level versus $\overline{\text{HRI}}$.

	Mean RMSE			
Coil type	Power law	Poly3	Ridge	Smoothing spline
SWRW	0.301	0.035	0.477	0.377
SWLW	0.673	1.595	1.520	1.063
HWRW	1.523	5.849	3.697	3.093

(1.4 °C rise), and 22.0 °C to 23.9 °C (1.9 °C rise), respectively. For the 166.5 mg ml^{-1} concentration (figure 7(c)), the heating profiles for SWRW, SWLW, and HWRW showed increases from 22.0 °C to 24.4 °C (2.4 °C rise), 21.9 °C to 24.1 °C (2.2 °C rise), and 22.0 °C to 24.5 °C (2.5 °C rise), respectively. All MNP traces exhibited a discrete 'staircase' morphology consistent with the 0.1 °C measurement system resolution. *BC* and N_{Steps} for each coil and concentration are summarized in table 3. *BC* remained below 7.1% across all conditions, indicating that the majority of the observed signal was attributable to MNP heating rather than environmental drift. In contrast, N_{Steps} ranged from 14 to 26 over the ∼40 min measurement window, corresponding to a τ_{Steps} of 1.5–2.8 min, indicating that sensor quantization, rather than environmental confounding, was the dominant limitation on the temporal resolution available for derivative-based SAR estimation. Applying the standard initial-slope SAR method (90 s window) to these data yielded unstable and, in several cases, physically implausible estimates (including negative apparent SAR values), as the initial window contained only 0–1 resolvable 0.1 °C temperature increments across all coil and concentration combinations, further confirming that sensor quantization, rather than the specific SAR extraction method, is the primary limitation on experimental calorimetry at this field intensity.

$\overline{\text{SAR}_1}$ for all tissue layers across all RF coils at 100% power level were below safety thresholds (figure 8(a)). Among the tissue layers, was lowest for the VCB and highest for the CSL, with the difference large enough to require a logarithmic scale for the bar charts. Inter-RF coil differences in $\overline{\text{SAR}_1}$ for the same tissue layer were minimal. $\bar{\Lambda}_{\text{SAR}}$ varied considerably across RF coils, while inter-tissue layer differences in $\bar{\Lambda}_{\text{SAR}}$ for the same RF coil were minimal (figure 8(b)). $\bar{\Lambda}_{\text{SAR}}$ was highest for HWRW and lowest for SWLW, showing a wide range across RF coils, requiring the same logarithmic scale. $\bar{\Lambda}_{\text{SAR}}$ for SWRW was also low, close to that of SWLW. See Tables S6–S8 for $\overline{\text{SAR}_1}$, $\overline{\text{SAR}_H}$, and $\bar{\Lambda}_{\text{SAR}}$ at all power levels.

4. Discussion

This study introduces a quantitative, reproducible framework for evaluating the electromagnetic quality of MH RF generator output. While RF coil design, cooling, MNP optimization, and thermal dosimetry have been extensively studied [35, 48–52], the electromagnetic fidelity of RF generators has received comparatively little attention.

Our results show that the HRI and $\overline{\text{HRI}}$ are sensitive, interpretable, and scalable indices for spectral purity across different RF coil designs, power levels, and spatial positions. The HRI maps (figures 5, S4–S6) and $\overline{\text{HRI}}$ trends (table 1 and figure 6) show monotonic increases with RF power for all coils, whereas THD and show weaker, spatially irregular variation with a narrower dynamic range, indicating lower sensitivity to spatially varying spectral impurities. This difference has direct physical relevance: eddy-current heating in conductive media scales approximately with f^2 [14, 15], so higher-order harmonics contribute disproportionately to parasitic losses despite similar amplitudes. THD (equation (11)) aggregates harmonic amplitudes without weighting by order and does not capture broadband spectral noise outside discrete harmonics. In contrast, HRI (equation (5)) incorporates harmonic order consistent with the f^2 scaling of eddy-current losses, making it more sensitive to higher-frequency components that dominate frequency-dependent losses [53]. Accordingly, HRI provides a physics-weighted

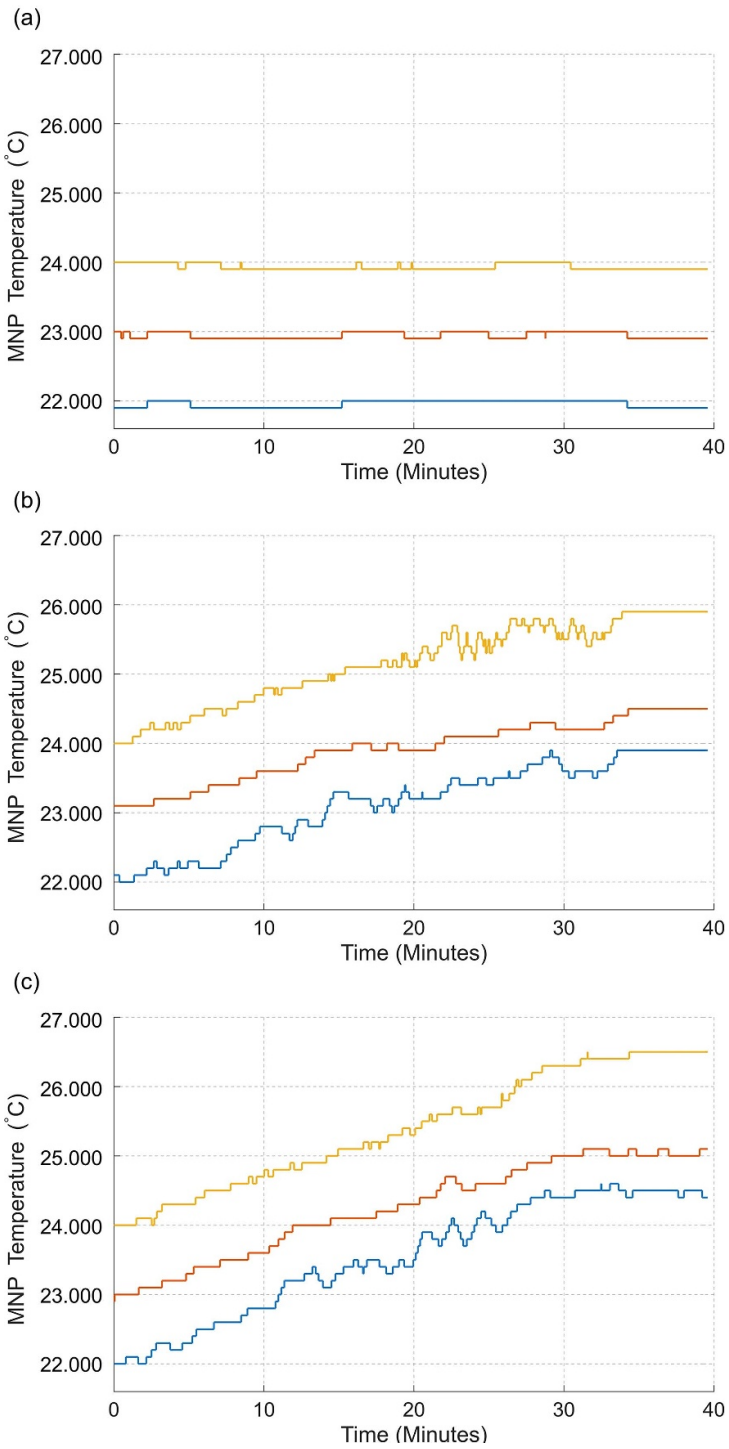

Figure 7. Comparative 40 min thermal traces for (a) distilled water control, (b) 120 mg ml^{-1}, and (c) 166.5 mg ml^{-1} MNP experiments. Traces correspond to SWRW (blue), SWLW (red), and HWRW (yellow) RF coils. For visual clarity, SWLW and HWRW traces in each subplot are vertically offset by 1.0 °C and 2.0 °C, respectively.

surrogate for relative susceptibility to parasitic eddy-current heating under comparable system conditions, whereas THD does not capture this frequency-dependent behaviour. This confirms that harmonic distortion primarily arises from RF generator nonlinearities rather than measurement artefacts or coil geometry [54]. The consistent vertical trend in HRI ($\pm$12 mm) across all coils and power levels matches expected edge-field effects near coil terminals [55], demonstrating spatial sensitivity and indicating that generator quality cannot be assessed from terminal-only measurements [56]. The power-law fit of $\overline{\mathrm{HRI}}$ (figure 6, table 1) shows a stable, monotonic relationship with power without overfitting.

Table 3. Background environmental contribution and sensor-resolution-limited temporal resolution for inductive heating measurements across RF coils and MNP concentrations. Background contribution was estimated as the distilled water control drift relative to the total MNP-induced temperature rise over the ∼40 min measurement window. Resolvable steps denote the number of distinct 0.1 °C increments detected by the fibre-optic sensor over the same window.

Coil type	MNP concentration (mg ml^{-1})	Total rise (°C)	Control drift (°C)	Background contribution (%)	Resolvable steps (∼40 min)	Step interval (min)
SWRW	120	1.8	0	0	19	2.08
	166.5	2.4	0	0	26	1.52
SWLW	120	1.4	−0.1	7.1	14	2.83
	166.5	2.2	−0.1	4.5	22	1.8
HWRW	120	1.9	−0.1	5.3	19	2.08
	166.5	2.5	−0.1	4	25	1.58

Methodologically, THD (equation (11)) aggregates harmonic amplitudes without frequency weighting, whereas HRI (equation (5)) emphasizes higher-order harmonics and includes a residual spectral term, capturing both harmonic and broadband distortion relevant to MH energy deposition [57, 58]. The harmonic term was restricted to odd orders consistent with Class-AB behaviour, but the formulation is readily extendable to include even-order components if needed.

Direct calorimetry for SAR estimation at clinical field intensities (5–10 kA m^{-1}) [30] is limited, as illustrated in figure 7 and quantified in table 3. Across both MNP concentrations, temperature rises remained $\leqslant$2.5 °C over the ∼40 min measurement window, producing a staircase response with only 14–26 resolvable 0.1 °C increments (mean step interval 1.5–2.8 min), which substantially constrains the temporal resolution available for derivative-based SAR estimation. Notably, background environmental contribution remained below 7.1% across all conditions (table 3). Contrary to typical assumptions about calorimetric MH dosimetry [31], this indicates that environmental and convective heat transfer were not the dominant limiting factor here; rather, sensor quantization was the primary constraint on resolving low-slope temperature derivatives. Importantly, MNP-specific SAR differs from tissue SAR, which represents bulk RF energy deposition relevant to safety limits such as IEEE C95.1 ($<$ 2 W kg^{-1}) [45]. This constraint was not limited to full-trace derivative approaches: applying the conventional initial-slope SAR method [31] over a standard 90 s window also yielded unstable and, in several cases, physically implausible estimates, as the window contained only 0–1 resolvable temperature increments. This indicates that the limitation is intrinsic to the measurement regime itself, rather than a specific artefact of the chosen analysis method. While MNP heating is intentionally maximized here, tissue SAR lies near the detection limits of indirect calorimetry, making results highly sensitive to sensor resolution constraints. This motivates FEM-based modelling, which directly computes localized SAR independent of thermal differentiation and provides a more robust framework for MH dosimetry. The present framework characterizes RF generator output quality and its coupling to tissue-level eddy-current SAR. The relationship between harmonic content and MNP-specific heating, governed by Néel and Brownian relaxation dynamics with a distinct frequency response [15–17], was outside the scope of this instrumentation-focused study and represents a direction for future work. Using SAR instead of heat flow directly captures electromagnetic interactions, making the indices independent of thermal experimental conditions [59]. Although HRI and show measurable harmonic content, FEM results indicate that $\overline{\mathrm{SAR}}_H$ is negligible compared to $\overline{\mathrm{SAR}}_1$ (Tables S6–S7). Even $\overline{\mathrm{SAR}}_1$ remains well below IEEE C95.1 limits [45] ($<$2 W kg^{-1}) across all coils and tissues (figure 8(a)). SAR is higher in NMT and CSL due to higher conductivity [47] and proximity to the coil [60], and lower in RBM and VCB. The $\bar{\Lambda}_{\mathrm{SAR}}$ metric shows total heating is dominated by the fundamental component, with highest values in HWRW, indicating minimal harmonic contribution due to weaker coupling to higher-order components [61].

The proposed indices provide a basis for future standardization in MH. Current reporting practices typically include only AMF amplitude–frequency and coil geometry, with limited information on spectral purity or RF generator nonlinearity. Our results show that measurable spectral deviations can occur even in well-designed systems and can be quantitatively characterized using the proposed framework. In this context, the development of standardized metrics for RF field characterization is an active area of research in biomedical electromagnetic systems, and analogous standardization challenges have been addressed in other imaging modalities such as MRI through formal intensity scale standardization methods [62], in addition to established exposure frameworks such as IEEE C95.1 [45] and ICNIRP [63] guidelines. Prior MH studies have also highlighted challenges in achieving consistent and comparable dosimetry due to methodological variability in SAR estimation [31]. To our knowledge, this is the first introduction of validated spectral quality indices for MH, addressing an overlooked source of variability

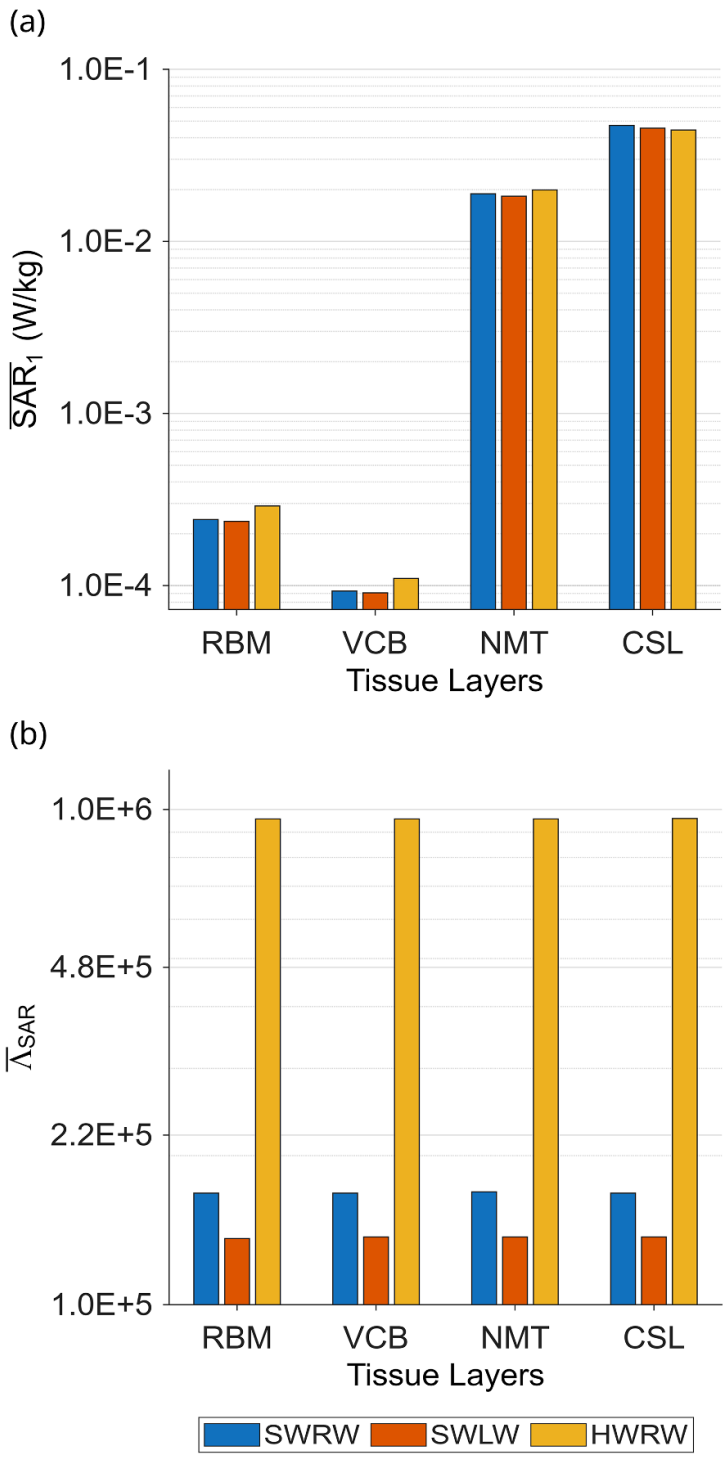

Figure 8. Grouped bar charts of (a) $\overline{SAR}_1$ (W kg^{-1}) and (b) for each tissue, with three RF coils at 100% power level.

in RF excitation systems. Standardized reporting of spectral purity would improve reproducibility, reduce simulation–experiment discrepancies, and support future regulatory translation.

This study has several limitations. Harmonic analysis was limited to odd-order components of a Class-AB system and may not capture all distortions from other inverter topologies, although the *HRI* framework itself is platform-independent. FEM simulations used a simplified four-layer neck model for worst-case SAR estimation rather than full anatomical detail. The study was performed at a single frequency (150 kHz), so absolute *HRI* values may vary with frequency, but the underlying frequency-weighted loss relationship remains valid with proper baseline calibration. Finally, reliance on simulation and spectral analysis over extensive calorimetry reflects the limited reliability of direct SAR extraction at low temperature rises ($\leqslant$ 2.5 °C) and sensor resolution constraints.

Future work should extend the $\mathrm{HRI} - \overline{\mathrm{HRI}}$ framework to alternative amplifier stage architectures, validate the $\bar{\Lambda}_{\mathrm{SAR}}$ index with anatomically more detailed models, incorporate real-time spectral purity monitoring into RF generator design and support the development of internationally adoptable MH hardware standards. By providing a quantitative link between generator output and localized SAR, this framework enables spectral purity to be evaluated as a relevant engineering parameter for generator design and quality control, offering a practical approach for quantifying effects that are difficult to resolve experimentally [20, 24–26].

While *HRI* provides a scalable measure of spectral purity, its interpretation depends on system-specific conditions. Higher *HRI* indicates dominance of the fundamental frequency, while lower values reflect increased harmonic content. Instead of universal thresholds, we propose using *HRI* as a baseline-referenced descriptor of nominal RF generator performance, established during system characterization. Deviations from this baseline indicate spectral degradation; stable agreement implies consistent operation, while reduced *HRI* suggests increased harmonic contamination requiring further evaluation. When harmonic components become significant, localized SAR assessment via FEM is recommended, with FEM analysis used as a second-stage validation when harmonic components become non-negligible in the measured spectrum. This baseline-based approach enables consistent, system-adaptive spectral assessment across MH platforms.

5. Conclusion

This study introduces the *HRI* as a sensitive, spatially resolved metric for quantifying the electromagnetic spectral purity of RF generators used in MH. Our findings demonstrate that while traditional *THD* lacks the frequency-order weighting and noise sensitivity required for high-precision dosimetry, the *HRI* provides a monotonic and predictable framework for hardware characterization across various RF coil geometries. The integration of experimental heating trials and FEM simulations further highlights the necessity of a simulation-based approach for SAR assessment. As physical measurements at clinical field intensities are inherently constrained by hardware resolution and marginal temperature elevations, the proposed simulation-based SAR assessment serves as a more reliable benchmark for characterizing electromagnetic output and supporting reproducibility in MH. By quantifying the spectral purity of the driving waveform, this methodology transforms generator fidelity from a secondary technical consideration into a quantifiable and standardisable engineering parameter for MH hardware design and quality control. Ultimately, this standardized spectral-quality reporting helps address an overlooked source of variability in RF excitation systems, providing a rigorous, reproducible benchmarking framework that can support future standardization efforts and more consistent electromagnetic output characterization across MH platforms.

Data availability statement

All data that support the findings of this study are included within the article (and any supplementary files).

Supplementary Data available at: https://doi.org/10.1088/1361-6463/ae9d8a/data1.

Conflict of interest

The authors declare that they have no known competing financial interests or personal relationships that could have appeared to influence the work reported in this paper.

Funding statement

This work was supported by the Boğaziçi University Research Fund under grant number 19661.

Ethics statement

This study does not involve human participants or animal subjects; therefore, ethical approval was not required.

Author contributions

Serhat Ilgaz Yöner 0000-0001-9262-8249
Conceptualization (lead), Formal analysis (lead), Methodology (lead), Software (lead), Writing – original draft (lead), Writing – review & editing (equal)

Alpay Özcan 0000-0002-3037-2812
Conceptualization (supporting), Funding acquisition (lead), Supervision (lead), Writing – review & editing (equal)

Oğuz Akın
Resources (supporting)

References

[1] Jordan A, Scholz R, Wust P, Fähling H and Felix R 1999 Magnetic fluid hyperthermia (MFH): cancer treatment with AC magnetic field induced excitation of biocompatible superparamagnetic nanoparticles *J. Magn. Magn. Mater.* **201** 413–9
[2] Rana P *et al* 2025 Magnetic hyperthermia-based therapies for cancer targeting: current progress and future perspectives *Med. Oncol.* **42** 453
[3] Szwed M and Marczak A 2024 Application of nanoparticles for magnetic hyperthermia for cancer treatment-the current state of knowledge *Cancers* **16** 1156
[4] Arbib S *et al* 2025 Extended treatment with magnetic nanoparticle hyperthermia in a "First-in-human" trial demonstrates safety and feasibility in an advanced cervical cancer case *J. Oncol. Res. Ther.* **10** 10304
[5] Kraus S *et al*. 2026 Case report: treatment with magnetic nanoparticle-based hyperthermia stabilizes metastatic disease in stage IV primary liver cancer patients. *Front. Oncol.* **15**
[6] Maier-hauff K, Ulrich F, Nestler D, Niehoff H, Wust P, Thiesen B, Orawa H, Budach V and Jordan A 2011 Efficacy and safety of intratumoral thermotherapy using magnetic iron-oxide nanoparticles combined with external beam radiotherapy on patients with recurrent glioblastoma multiforme *J. Neurooncol.* **103** 317–24
[7] Wlodarczyk A, Gorgon S, Radon A and Bajdak-rusinek K 2022 Magnetite nanoparticles in magnetic hyperthermia and cancer therapies: challenges and perspectives *Nanomaterials* **12** 1807
[8] Drake P, Algaddafi A, Swift T and Abd-alhameed R A 2024 Design and modelling of an induction heating coil to investigate the thermal response of magnetic nanoparticles for hyperthermia applications *BioMedInformatics* **4** 1006
[9] Ludwig R and Bogdanov G 2000 *RF Circuit Design: Theory & Applications* 2nd edn (Pearson)
[10] Zhang Y and Lu M 2024 Advances in magnetic induction hyperthermia *Front. Bioeng. Biotechnol.* **12** 1432189
[11] Atkinson W J, Brezovich I A and Chakraborty D P 1984 Usable frequencies in hyperthermia with thermal seeds *IEEE Trans. Biomed. Eng.* **31** 70–75
[12] Kwok M K Y, Maley C C J, Dworkin A, Hattersley S, Southern P and Pankhurst P A 2023 Nonspecific eddy current heating in magnetic field hyperthermia *Appl. Phys. Lett.* **122** 240502
[13] Greenebaum B and Barnes F 2022 *Biological and Medical Aspects of Electromagnetic Fields* (CRC Press)
[14] Dutz S and Hergt R 2013 Magnetic nanoparticle heating and heat transfer on a microscale: basic principles, realities and physical limitations of hyperthermia for tumour therapy *Int. J. Hyperthermia* **29** 790–800
[15] Stigliano R V, Shubitidze F, Petryk J D, Shoshiashvili L, Petryk A A and Hoopes P J 2016 Mitigation of eddy current heating during magnetic nanoparticle hyperthermia therapy *Int. J. Hyperthermia* **32** 735–48
[16] Stoner E C and Wohlfarth E P 1991 A mechanism of magnetic hysteresis in heterogeneous alloys *IEEE Trans. Magn.* **27** 3475–518
[17] Debye P J W 1929 *Polar molecules* (The Chemical Catalog Company, Inc.) (available at: https://library.plu.edu/discovery/fulldisplay/alma991145333406356/01PACLUTH_INST:PACLUTH)
[18] Shliomis M I 1974 Magnetic fluids *Sov. Phys. Usp.* **17** 153
[19] Johannsen M, Gneveckow U, Eckelt L, Feussner A, Waldöfner N, Scholz R, Deger S, Wust P, Loening S A and Jordan A 2005 Clinical hyperthermia of prostate cancer using magnetic nanoparticles: presentation of a new interstitial technique *Int. J. Hyperthermia* **21** 637–47
[20] Wells J *et al* 2021 Challenges and recommendations for magnetic hyperthermia characterization measurements *Int. J. Hyperthermia* **38** 447–60
[21] Al-dayeh L, Rahman M and Venook R 2020 Practical aspects of MR imaging safety test methods for MR conditional active implantable medical devices *Magn. Reson. Imaging Clin. N. Am.* **28** 559–71
[22] Dums J F, Schneider B J and Badin A A 2017 Low cost system to measure active power in electrosurgical units *Res. Biomed. Eng.* **33** 313–23
[23] Mild K H, Lundström R and Wilén J 2019 Non-ionizing radiation in Swedish health care-exposure and safety aspects *Int. J. Environ. Res. Public Health* **16** 1186
[24] International Electrotechnical Commission 2022 IEC 60601-2-33:2022 (International Electrotechnical Commission)
[25] International Electrotechnical Commission 2017 IEC 60601-2-2:2017 (International Electrotechnical Commission)
[26] International Electrotechnical Commission 2012 IEC 60601-1-8:2006/AMD1:2012 (International Electrotechnical Commission)

[27] Zeinoun M, Domingo-diez J, Rodriguez-garcia M, Garcia O, Vasic M, Ramos M and Serrano Olmedo J J 2021 Enhancing magnetic hyperthermia nanoparticle heating efficiency with non-sinusoidal alternating magnetic field waveforms *Nanomaterials* **11** 3240
[28] Barrera G, Allia P and Tiberto P 2020 Fine tuning and optimization of magnetic hyperthermia treatments using versatile trapezoidal driving-field waveforms *Nanoscale Adv.* **2** 4652–64
[29] Sharma A *et al* 2023 Validation of a temperature-feedback controlled automated magnetic hyperthermia therapy device *Cancers* **15** 327
[30] Pankhurst Q A, Thanh N T K, Jones S K and Dobson J 2009 Progress in applications of magnetic nanoparticles in biomedicine *J. Phys. D: Appl. Phys.* **42** 224001
[31] Wildeboer R R, Southern P and Pankhurst Q A 2014 On the reliable measurement of specific absorption rates and intrinsic loss parameters in magnetic hyperthermia materials *J. Phys. D: Appl. Phys.* **47** 495003
[32] Grattan K T V and Sun T 2000 Fiber optic sensor technology: an overview *Sensors Actuators A* **82** 40–61
[33] Yoner S I 2025 *Design and Optimization of a Nanoparticle Based Magnetic Hyperthermia Device* (Boğaziçi University)
[34] Attaluri A, Jackowski J, Sharma A, Kandala S K, Nemkov V, Yakey C, DeWeese T L, Kumar A, Goldstein R C and Ivkov R 2020 Design and construction of a Maxwell-type induction coil for magnetic nanoparticle hyperthermia *Int. J. Hyperthermia* **37** 1–14
[35] García O *et al* 2016 Development and testing of a new instrument for researching on cancer treatment technologies based on magnetic hyperthermia *IEEE J. Emerg. Sel. Top. Power Electron.* **4** 243–51
[36] Hewlett W R A 1939 *A New Type of Resistance-Capacitance Oscillator* (Stanford University)
[37] Sedra A S and Smith K C 2015 *Microelectronic Circuits* 7th edn (Oxford University Press)
[38] Analog Devices 2009 MT-101: decoupling Techniques
[39] Bowick C 1982 *RF Circuit Design* 2nd edn (Newnes)
[40] Pozar D M 1990 *Microwave Engineering* 1st edn (Addison-Wesley)
[41] Faraday M 1832 Experimental Researches in Electricity *Philos. Trans. R. Soc.* **122** 125–62
[42] Vuolevi J and Rahkonen T 2003 Distortion in RF power amplifiers (Artech)
[43] Gabriel S, Lau R W and Gabriel C 1996 The dielectric properties of biological tissues: II. Measurements in the frequency range 10 Hz to 20 GHz *Phys. Med. Biol.* **41** 2251–69
[44] Papoulis A *et al* 2002 *Random Variables, and Stochastic Processes* 4th (McGraw-Hill)
[45] Institute of Electrical and Electronics Engineers 2019 IEEE standard C95.1-2019: safety levels with respect to human exposure to electric, magnetic, and electromagnetic fields, 0 Hz to 300 GHz
[46] Reddy J N 2006 *An Introduction to the Finite Element Method* 4th edn (McGraw Hill)
[47] Total Materia Database 2023 Total Materia - Where Material Information Meets Design, Innovation and Sustainability (available at: www.totalmateria.com/) (Accessed 9 February 2026)
[48] Yoner S I and Ozcan A 2025 Simulation-based design and machine learning optimization of a novel liquid cooling system for radio frequency coils in magnetic hyperthermia *Bioengineering* **12** 490
[49] Socoliuc V, Peddis D, Petrenko V I, Avdeev M V, Susan-resiga D, Szabó T, Turcu R, Tombácz E and Vékás L 2020 Magnetic nanoparticle systems for nanomedicine—a materials science perspective *Magnetochemistry* **6** 2
[50] Gavilán H, Avugadda S K, Fernández-cabada T, Soni N, Cassani M, Mai B T, Chantrell R and Pellegrino T 2021 Magnetic nanoparticles and clusters for magnetic hyperthermia: optimizing their heat performance and developing combinatorial therapies to tackle cancer *Chem. Soc. Rev.* **50** 11614–67
[51] Rodriguez B, Rivera D, Zhang J Y, Brown C, Young T, Williams T, Huq S, Mattioli M, Bouras A and Hadjpanayis C G 2024 Magnetic hyperthermia therapy for high-grade glioma: a state-of-the-art review *Pharmaceuticals* **17** 300
[52] Baldea I, Iacoviță C, Gurgu R A, Vizitiu A S, Râzniceanu V and Mitrea D R 2025 Magnetic hyperthermia with iron oxide nanoparticles: from toxicity challenges to cancer applications *Nanomaterials* **15** 1519
[53] Lin J C 2006 A new IEEE standard for safety levels with respect to human exposure to radio-frequency radiation *IEEE Antennas Propag. Mag.* **48** 157–9
[54] Self D 2006 *Audio Power Amplifier Design Handbook* 4th edn (Newnes)
[55] Kazimierczuk M K 2014 *High-Frequency Magnetic Components* 2nd edn (Wiley)
[56] Lee S K, Oh S, Kim H S and Song B P 2021 Radio-frequency vector magnetic field mapping in magnetic resonance imaging *IEEE Trans. Med. Imaging* **40** 963–73
[57] Bassesuka A and Nzao S 2021 Study and modeling of human biological tissue exposed to high frequency electromagnetic waves *Open J. Appl. Sci.* **11** 1109–21
[58] Federal Office for Radiation Protection (BfS) 2025 Biological effects of radiofrequency electromagnetic fields due to energy absorption and heating (available at: www.bfs.de/EN/topics/emf/hff/effect/hff-established/hff-established_node.html)
[59] Panagopoulos D J, Johansson O and Carlo G L 2013 Evaluation of specific absorption rate as a dosimetric quantity for electromagnetic fields bioeffects *PLoS One* **8** e62663
[60] Jackson J D 1998 *Classical Electrodynamics* 3rd edn (Wiley)
[61] Ciappina M F, Biegert J, Quidant R and Lewenstein M 2012 High-order-harmonic generation from inhomogeneous fields *Phys. Rev. A* **85** 033828
[62] Nyul L G, Udupa J K and Zhang X 2000 New variants of a method of MRI scale standardization *IEEE Trans. Med. Imaging* **19** 143–50
[63] ICNIRP ICoN-IRP 2020 Guidelines for limiting exposure to electromagnetic fields *Health Phys.* **118** 483–524